Available online at www.sciencedirect.com
ScienceDirect
Trans. Nonferrous Met. Soc. China 32(2022) 3349−3361
Transactions of Nonferrous Metals Society of China
www.tnmsc.cn

High-temperature thermal stability of C/C−ZrC−SiC composites via region labeling method

Zheng PENG[1], Chun-mao MIAO[1], Wei SUN[1], Yong-long XU[1], Hai-kun CHEN[2], Yu-feng LIU[2], Hong-bo ZHANG[1], Xiang XIONG[1]

1. State Key Laboratory of Powder Metallurgy, Central South University, Changsha 410083, China;
2. Science and Technology on Advanced Functional Composites Laboratory, Aerospace Research Institute of Materials and Processing Technology, Beijing 100089, China

Received 13 August 2021; accepted 28 April 2022

Abstract: To investigate the thermal stability of ceramic-matrix composites, three kinds of C/C−ZrC−SiC composites with different Zr/Si molar ratios were synthesized by reactive melt infiltration. Employing region labeling method, the high-temperature thermal stability of the composites was systematically studied by changing the temperature and holding time of thermal treatment. Results show that the mass loss rate of low Si composites has a growth trend with increasing temperature, and a crystal transformation from β-SiC to α-SiC occurs in the composites. In the calibrated area, SiC phase experiences Ostwald ripening and volume change with location migration, while ZrC phase experiences a re-sintering process with diffusion. Moreover, it is found that increasing temperature has a more obvious effect on the thermal stability than extending holding time, which is mainly attributed to the faster diffusion rate of atoms.

Key words: thermal stability; ceramic-matrix composites; reactive melt infiltration; high-temperature thermal treatment; region labeling method

1 Introduction

The thermal structural materials used in hypersonic vehicles need to withstand harsh environments with ultra-high temperature airflow, so the properties of ablation resistance and thermal stability are extremely important [1]. The most commonly used thermal structural materials are refractory metals, C/C composites, and ceramic-matrix composites. Among them, ceramic-matrix composites have the advantages of good chemical stability, excellent oxidation resistance and low thermal conductivity, making them as the promising candidates for high temperature applications [2−5]. Especially, the C/C−ZrC−SiC composites have received considerable attention for their superior ablation-resistant properties, as the dense protective layer of ZrO_2 and SiO_2 could be formed to effectively protect the substrate under the oxygen-containing environment [6−9]. At present, the main methods to prepare the C/C−ZrC−SiC composites are chemical vapor deposition (CVD), precursor infiltration and pyrolysis (PIP), and reactive melt infiltration (RMI). Reactive melt infiltration is one of the most industrially competitive methods with the merits of low cost and short process cycle. Besides, the materials prepared by RMI have low porosity and can achieve a near-net shape [10,11]. However, the ceramic phases in C/C−ZrC−SiC composites prepared by RMI would undergo series of evolution in high-temperature environments. Therefore, it is necessary to research the high-temperature thermal stability of C/C−ZrC−SiC composites for the engineering application references.

Corresponding author: Wei SUN, Tel: +86-13808478540, E-mail: sunweimse@csu.edu.cn
DOI: 10.1016/S1003-6326(22)66024-2

Previous studies [12−14] showed that high-temperature thermal treatment could make a difference in microstructures of ceramic-matrix composites, which would affect their mechanical and ablation properties. CHEN et al [12] studied the effects of high-temperature annealing on the microstructures and properties of C/SiC−ZrB_2 composites. They found that as the annealing temperature increased, the crystallization degree of the amorphous SiC increased. MEI et al [13] and QIN et al [14] studied the effects of heat treatment temperature on microstructures and mechanical properties of chopped carbon fiber SiC composites. It was found that a proper treatment temperature could improve the mechanical properties of composites. Besides, there have been other reports on the thermal stability behaviors with high-temperature treatment [15−19]. YU et al [20] and JIA [21] researched the high-temperature thermal stability of ZrC in W/ZrC cermets under different treatment conditions, and found that there was mutual diffusion behavior between ZrC and W, which affected the initial crystal structures and grain sizes. XIE et al [22] studied the effect of annealing treatment on the phase transformation of SiC ceramics. However, there is a lack of systematic research on the high-temperature thermal stability behaviors of C/C−ZrC−SiC composites. What's more, scholars have not employed the region labeling method to in-situ characterize the specific area before and after high-temperature thermal treatment so far.

Thus, in this work, the region labeling method has been employed to research the effects of temperature and holding time on the thermal stability of C/C−ZrC−SiC composites. The overall high-temperature thermal stability was systematically studied and four evolution models were developed based on experimental results.

2 Experimental

In the experiment, 2.5D acupuncture porous C/C composites were used as substrate. They were densified through the CVI process, which used methane as the carbon source gas and hydrogen and nitrogen as the carrier gases. Then, Zr powder (Haotian Titanium Powder Processing Co., Ltd., Jinzhou, China) and Si powder (Xingrongyuan Technology Co., Ltd., Beijing, China) with a purity of 99.9% were mixed and ball milled with alcohol in a tumbling mill (XQM, Kexi Institute of Experimental Instruments) for 24 h, followed by blast drying. The low-Si (LSi) and high-Si (HSi) systems of C/C−ZrC−SiC composites with different proportions of Zr−Si powders are listed in Table 1. In the case of molten salt assisted (NaCl) samples, NaCl (China National Pharmaceutical Group Chemical Reagent Co., Ltd., Shanghai) and Zr−Si mixed powder were selected as the infiltration masterbatch, with a mass ratio of 8:100. The C/C composites were embedded in the infiltration masterbatch, using graphite crucibles as the vessel for RMI process. The samples were heated to 2000 °C at a heating rate of 10 °C/min and kept at 2000 °C for 2 h.

After the RMI process, three types of C/C−ZrC−SiC composites were processed into round blocks with a diameter of 28−30 mm and a thickness of 10 mm. Then, they were cut across a groove with a depth of 1−2 mm and a width of 2 mm, followed by a groove with a depth of 1 mm and a width of 2 mm on the side. Thus, the orientations of samples were marked, and four detection areas were calibrated. Figure 1 shows the schematic diagram of region labeling method. During the thermal treatment with graphitization furnace, the calibrated samples were placed in

Table 1 High-temperature thermal treatment parameters for different C/C−ZrC−SiC composites

System	Sample	Content/wt.%		Treatment temperature/°C	Treatment time/h
		Zr	Si		
Low-Si	LSi21	70	30	2000	3
	LSi31	70	30	2300	3
	LSi22	70	30	2000	24
High-Si	HSi21	50	50	2000	3
Molten salt assisted	NaCl21 (8 wt.% NaCl)	70	30	2000	3

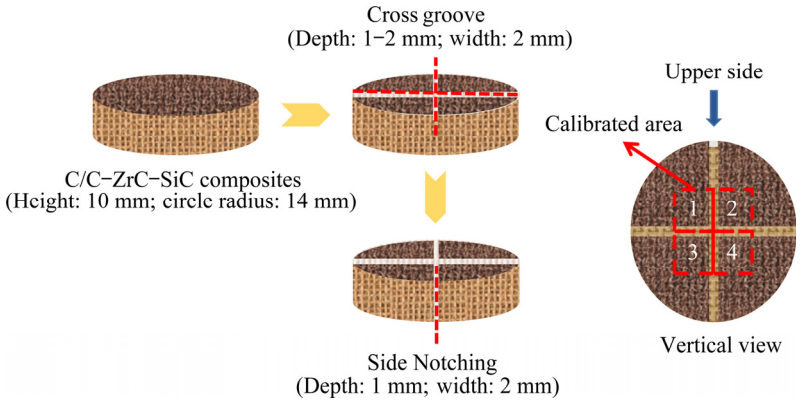

Fig. 1 Schematic diagram of region labeling method

different graphite crucibles and sealed with C paper. Besides, Ar was used as a protective gas.

The phase analysis of the C/C−ZrC−SiC composites before and after thermal treatment was performed using an X-ray diffraction (XRD) analyzer (D/max 2550 vb + 18 kW, Rigaku Co., Japan). The microstructures of composites were analyzed using a scanning electron microscopy (SEM, NanoSEM230, Novtma, Holland). The elemental analysis was investigated by an electron probe micro-analyzer (EPMA, JXA−8530F, JEOL, Japan).

3 Results and discussion

3.1 Thermal stability of C/C−ZrC−SiC composites

Overall, the C/C−ZrC−SiC composites have experienced the mass loss and thickness growth during high-temperature thermal treatment, as illustrated in Fig. 2.

The main reasons for the mass loss and thickness growth are as follows: the residual Si in the C/C−ZrC−SiC composites will be volatilized at 2000 °C during high-temperature treatment, which

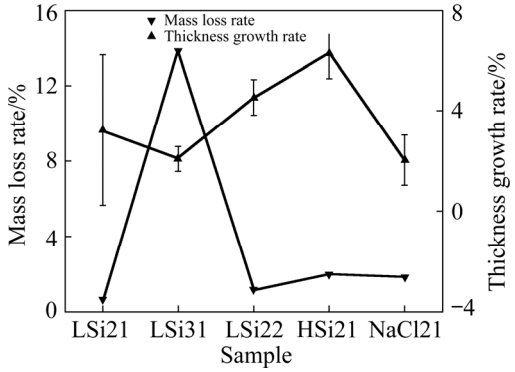

Fig. 2 Mass loss rate and thickness growth rate during thermal treatment for different C/C−ZrC−SiC composites

accounts for the quality loss. When the temperature rises to 2300 °C, the decomposition Reaction (1) will occur as well, causing a large amount of Si to be lost in the form of steam [23]. Besides, the thickness increase of composites during thermal treatment is based on the grain growth and organization migration of ceramic phases.

$$SiC(s)=Si(g)+C(s) \quad (1)$$

What's more, different factors have distinct effects on the thermal stability behaviors. On the one hand, as the temperature increases, the mass loss rate of C/C−ZrC−SiC composites shows a significant growth trend, reaching 13.806% at 2300 °C (LSi31), which is about 22 times more than that at 2000 °C (LSi21), while the thickness growth rate shows a downward trend with the increase of temperature from 2000 to 2300 °C. On the other hand, the mass loss rate and thickness growth rate show upward trends with increasing holding time, as evidenced in LSi21 and LSi22. Besides, increasing Si content in the infiltration masterbatch, both the mass loss rate and thickness growth rate show upward trends after high-temperature treatment. The thickness growth rate of HSi21 is the highest among all composites, reaching about 6.286%. Furthermore, incorporated with the NaCl molten salt, the mass loss rate of NaCl21 composites shows an upward trend, but the thickness growth rate shows a downward trend compared to LSi21 composites.

3.2 Effect of heat treatment parameters on high-temperature thermal stability

3.2.1 Effect of temperature

Figure 3 shows the XRD patterns of LSi21

and LSi31 composites before and after thermal treatment. After thermal treatment at above 2000 °C, the peaks of C, ZrC, and SiC in LSi21 and LSi31 composites are shifted. Besides, the crystal transformation from β-SiC to α-SiC is observed [24,25], as the diffraction peaks of α-SiC appears. To be more specific, the angle of main diffraction peak (111) of β-SiC in LSi21 shifts from 35.623° (d=2.5182 Å, d is the crystal plane spacing) to 35.663° (d=2.5155 Å), and the peaks of α-SiC exist at 34.101° (d=2.6270 Å) and 38.155° (d=2.3567 Å). According to the Bragg diffraction equation (Eq. (2)), the crystal plane spacing is inversely proportional to the diffraction peak angle. The diffraction peaks of β-SiC shift to larger angles, which illustrates that the interplanar spacing has a decreasing trend. When the treatment temperature increases to 2300 °C, the diffraction peak of β-SiC in LSi31 almost completely disappears, and the α-SiC peaks appear at 34.143° (d=2.6238 Å) and 34.933° (d=2.5663 Å).

$$2d\sin\theta=n\lambda \tag{2}$$

where θ is the angle between the incident X-ray and the corresponding crystal plane, which is equal to half of the diffraction peak angle 2θ; n(=1, 2, 3, ⋯) is the order of diffraction; λ is the incident wavelength. In this study, a Cu target is selected for XRD, and λ is 0.154056 nm.

Furthermore, as exhibited in Fig. 3, the angles of (111) and (200) diffraction peaks of ZrC in LSi21 shift from 32.976° (d=2.7141 Å) and 38.270° (d=2.3499 Å) to 33.056° (d=2.7076 Å) and 38.331° (d=2.3463 Å), respectively. Meanwhile, the angles of (111) and (200) diffraction peaks of ZrC in LSi31 shift from 32.976° (d=2.7141 Å) and 38.271° (d=2.3498 Å) to 33.074° (d=2.7062 Å) and 38.351° (d=2.3451 Å), respectively.

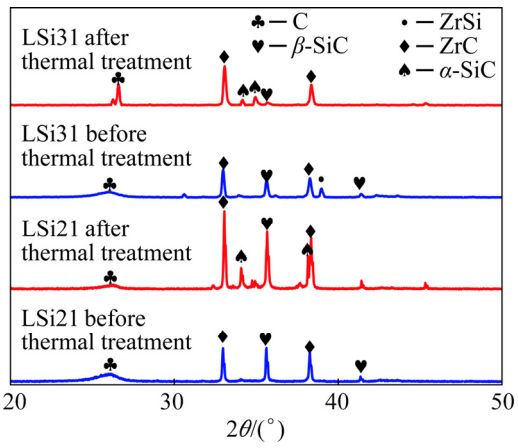

Fig. 3 XRD patterns of LSi21 and LSi31 composites before and after thermal treatment

At different thermal treatment temperatures, the SiC phase in the calibrated areas shows different microstructural evolution and migration behaviors. It can be seen that when the treatment temperature is 2000 °C, a few SiC grains in LSi21 sample grow from irregularly shaped bulk crystals (Zone I in Fig. 4(a)) into regular block crystals with distinct edges, corners, and flat crystal faces (Zone III in Fig. 4(c)). When the treatment temperature reaches up to 2300 °C, the number of SiC grains in the calibration area is significantly reduced (Fig. 4(d)). These SiC grains are not continuous, and almost all of them change from irregular shapes (Zone II in Fig. 4(b)) to hexagonal prisms or hexagonal pyramids (Zone IV in Fig. 4(d)). These hexagonal prisms or hexagonal pyramids conform to the hexagonal crystal structure of α-SiC. Therefore, the degree of crystal transformation of SiC phase increases with treatment temperature rising. In addition, it can be seen that the maximum grain size of SiC in the calibrated area at 2000 °C is 80−100 μm (Fig. 4(c)), while the size of SiC grains is much greater in the case of 2300 °C, and the maximum size exceeds 200 μm (Fig. 4(d)). The abnormal growth of large SiC grains at the cost of small grains conforms to the Ostwald ripening mechanism [26,27]. Based on the grain growth rate (Eq. (3)), the higher the treatment temperature, the faster the grain growth rate and the larger the crystallite size. Thus, as treatment temperature increases, the Ostwald ripening degree of SiC phase increases.

$$u=u_0\exp[-Q/(RT)] \tag{3}$$

where u is the grain growth rate; u_0 is a constant related to the atomic transition; Q is the activation energy; R is the molar gas constant; T is the thermodynamic temperature.

Furthermore, the exposed C fiber area on the surface of LSi21 decreases after thermal treatment at 2000 °C, and a ceramic layer with small grain size appears. For the reasons, on the one hand, these crystal grains are related to the reaction of low melting ZrSi and Si with C. On the other hand, the ceramic phases migrate from the fiber bundle layer to the surface of composite. During the thermal treatment at 2300 °C, the degree of Ostwald

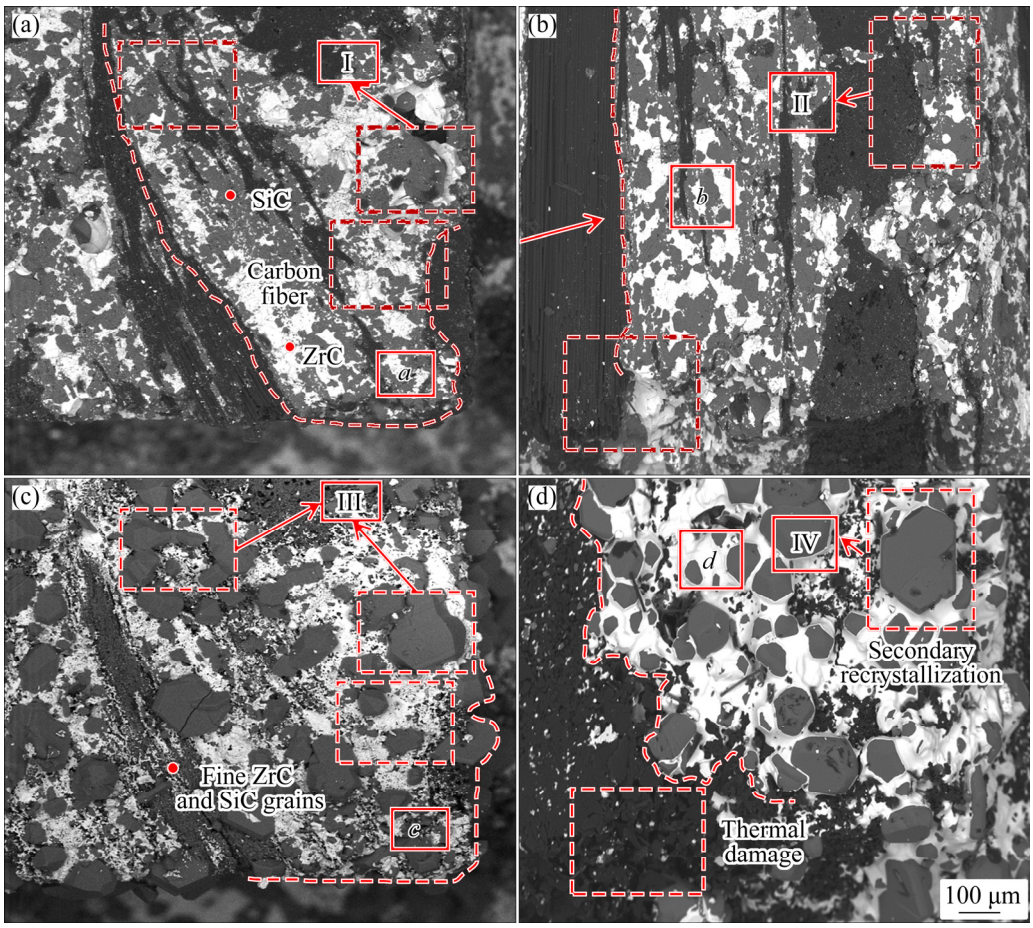

Fig. 4 SEM images of LSi21 and LSi31 before and after thermal treatment: (a) LSi21 before thermal treatment; (b) LSi31 before thermal treatment; (c) LSi21 after thermal treatment; (d) LSi31 after thermal treatment

ripening of SiC in LSi31 is too high, which leads to the destruction of continuous ceramic phase structure. The change of the C diffraction peak before and after the high-temperature treatment in Fig. 3 is consistent with the microstructure evolution of SiC in LSi21 and LSi31. The area of C diffraction peak in LSi21 is significantly reduced, which proves that the C fiber distributed on the surface is reduced, while the C diffraction peak in LSi31 becomes sharper because of the crystallization of free C or pyrolytic C.

Meanwhile, Fig. 4 depicts the high-temperature thermal stability behaviors of ZrC in the calibrated areas of LSi21 and LSi31. As the temperature increases, the migration behavior of ZrC grains along the parallel surface direction becomes more obvious. Besides, it can be seen that after high-temperature treatment, the ZrC phase in the LSi21 sample exhibits grain refinement, as shown in Figs. 5(a) and (c); while some of ZrC in the calibrated area of LSi31 changes from discontinuous irregular block crystals to continuous lamellar crystals, and a typical layered stacked structure appears on the surface (Figs. 5(b) and (d)) [28]. The interfaces between adjacent ZrC grains are obvious, forming a ravine morphology that is similar to the thermal etch angle. The microstructural evolution and migration of ZrC conform to the re-sintering behaviors, which manifests as the single structure being merged together during high-temperature treatment.

3.2.2 Effect of holding time

Figure 6 shows the XRD patterns of LSi21 and LSi22 before and after high-temperature thermal treatment. The angle of main diffraction peak (111) of β-SiC in LSi22 shifts from 35.722° (d=2.5114 Å) to 35.547° (d=2.5234 Å), and the peaks of α-SiC appear at 37.782° (d=2.3791 Å) and 41.395° (d=2.1794 Å) as time passes. Meanwhile, the angles of (111) and (200) diffraction peaks of ZrC in LSi22

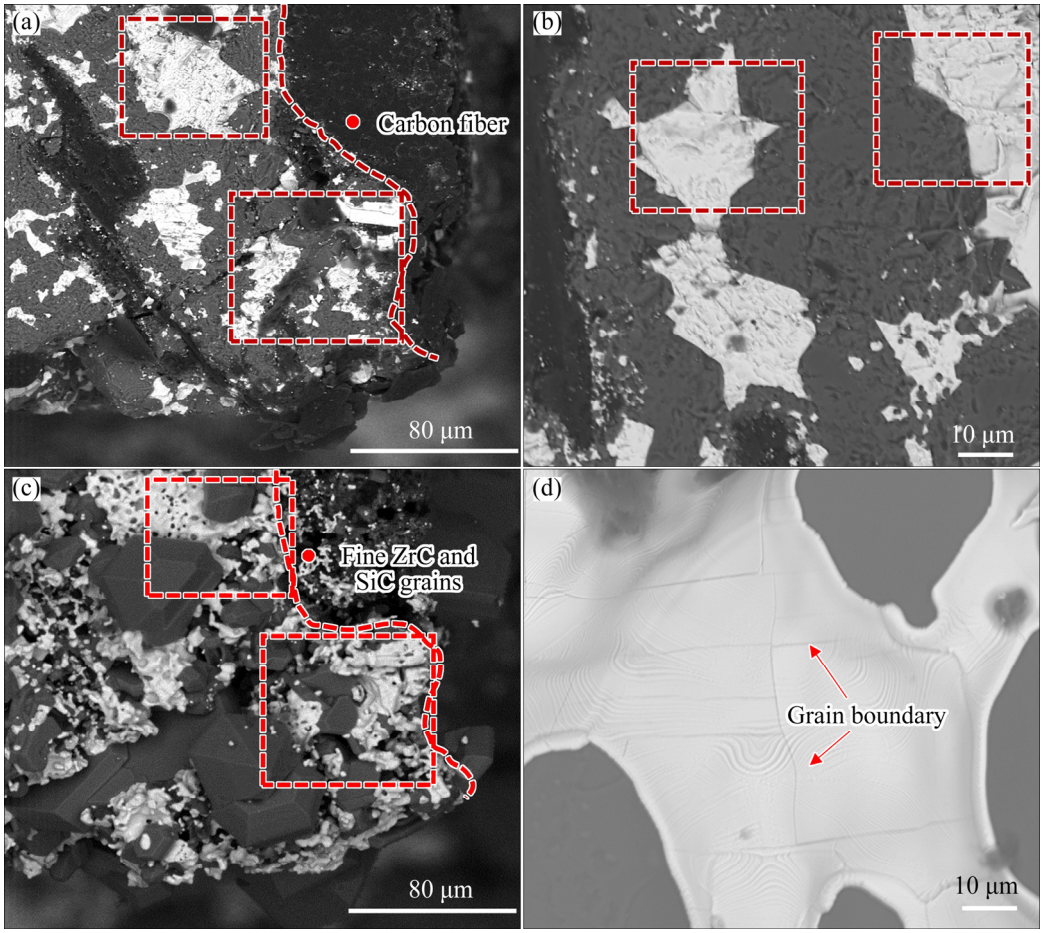

Fig. 5 SEM images of LSi21 and LSi31 before and after high-temperature treatment: (a) Enlarged view of Area *a* in Fig. 4(a); (b) Enlarged view of Area *b* in Fig. 4(b); (c) Enlarged view of Area *c* in Fig. 4(c); (d) Enlarged view of Area *d* in Fig. 4(d)

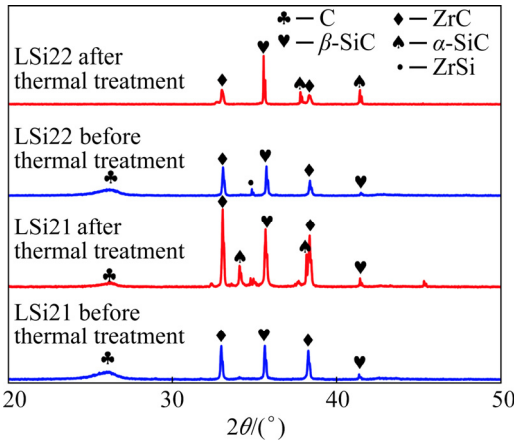

Fig. 6 XRD patterns of LSi21 and LSi22 before and after thermal treatment

shift from 33.076° (*d*=2.7060 Å) and 38.352° (*d*=2.3450 Å) to 33.034° (*d*=2.7094 Å) and 38.331° (*d*=2.3463 Å), respectively. According to the Brook model (Eq. (4)), it is assumed that the initial grain size remains unchanged and the grain size is proportional to time:

$$G^{n_1} - G_0^{n_1} = Kt \tag{4}$$

where G is the grain size; G_0 is the initial grain size; n_1 is the grain growth kinetic index, where the smaller the value, the easier the growth; t is time. K follows the Arrhenius law (Eq. (5)), and when the temperature remains constant, K does not change:

$$K=K_0\exp[-Q/(RT)] \tag{5}$$

where K_0 is a constant related to atomic migration. Therefore, as the holding time increases, the crystal grain size increases. The grain growth behavior in the C/C−ZrC−SiC composites with low Si content conforms to this law (Fig. 7).

As shown in Fig. 7, during 24 h treatment at 2000 °C, the abnormally grown SiC grains appear in the calibrated area of LSi22, and the maximum grain size is approximately 150 μm, which is larger than that of LSi21. Furthermore, it can be seen that the ceramic phase and C fiber are alternately

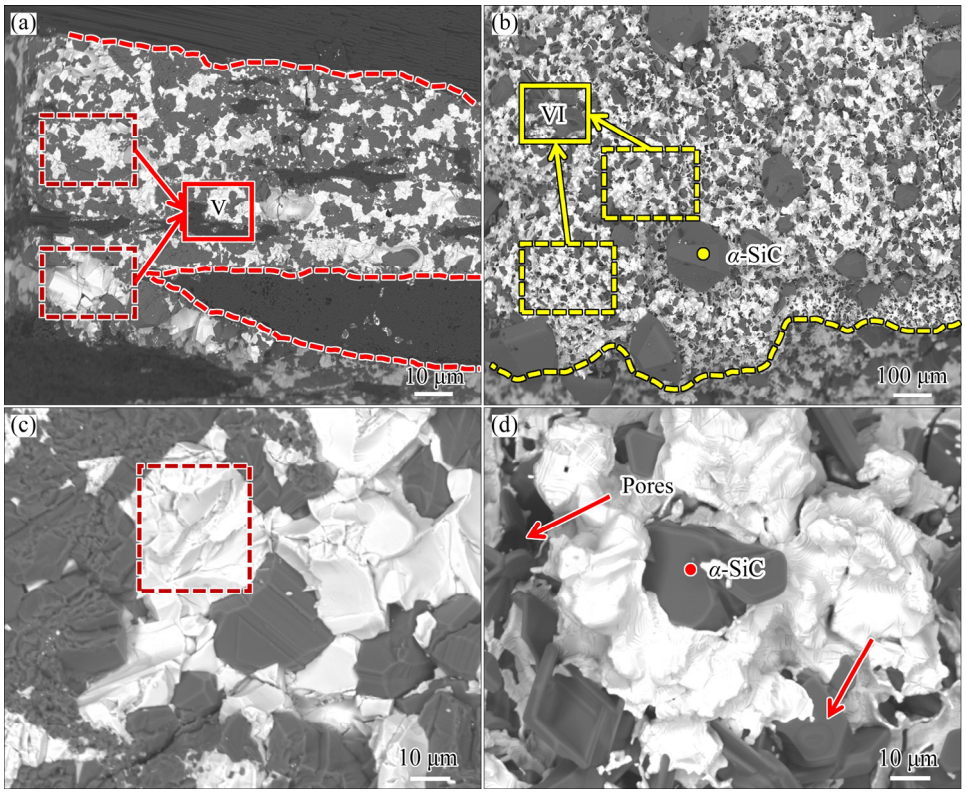

Fig. 7 SEM images of LSi22 before and after high-temperature treatment: (a) LSi22 before thermal treatment; (b) LSi22 after thermal treatment; (c) Enlarged view of (a); (d) Enlarged view of (b)

distributed in the calibrated area of LSi22 before treatment. While after 24 h treatment, the calibrated area of LSi22 is completely covered by a ceramic phase layer of SiC and ZrC. At the top of the ceramic phase layer there are a few large SiC grains that have grown abnormally owing to Ostwald ripening. These large crystal grains are completely transformed into hexagonal pyramid-shaped α-SiC. Besides, as shown in Fig. 7(d), the SiC grains that constitute the framework of ceramic phase layer also undergo the crystalline transformation, accompanied by the shape and volume changes, so the ceramic phase layer has some pore channels.

What's more, the ZrC in the calibrated area of LSi22 changes from a discontinuous block structure (Zone V in Fig. 7(a)) to a continuous lamellar structure (Zone VI in Fig. 7(b)) after thermal treatment. The evolution and migration of ZrC grains in LSi22 are similar to those of ZrC grains in LSi31. The difference is that the densification of ZrC in the LSi22 only appears in a small region around the SiC grains.

3.2.3 Other influencing factors

Figure 8 shows the XRD patterns of LSi21, HSi21 and NaCl21 before and after high-temperature treatment. During thermal treatment at 2000 °C for 3 h, the angle of main diffraction peak (111) of β-SiC in HSi21 shifts from 35.663° (d=2.5155 Å) to 35.546° (d=2.5235 Å), and that shifts from 35.644° (d=2.5168 Å) to 35.624° (d=2.5181 Å) in NaCl21 sample. With increasing Si content in the infiltration masterbatch, the diffraction peak of β-SiC shifts from a large angle to a small angle and the interplanar spacing shows a increasing trend.

In addition, the changes of average grain sizes for SiC before and after high-temperature treatment in LSi21, HSi21, and NaCl21 could be obtained according to Eq. (6). With calculation, the average grain sizes of SiC in LSi21, HSi21 and NaCl21 all show the decreasing trend. Among them, HSi21 has the largest decrease, being reduced to 37.478 nm.

$$D=\frac{K_1\lambda}{\beta\cos\theta} \tag{6}$$

where D is the average grain size; K_1 is the Scherrer constant, which has a value of 0.89; β is the half-height width.

Figure 9 presents the SEM images of HSi21 and NaCl21 before and after high-temperature

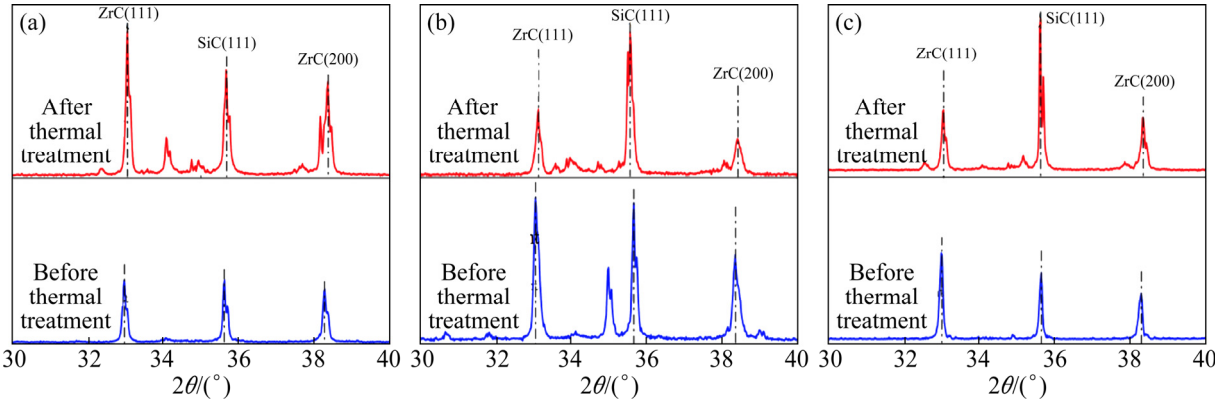

Fig. 8 XRD patterns of LSi21 (a), HSi21 (b) and NaCl21 (c) before and after high-temperature treatment

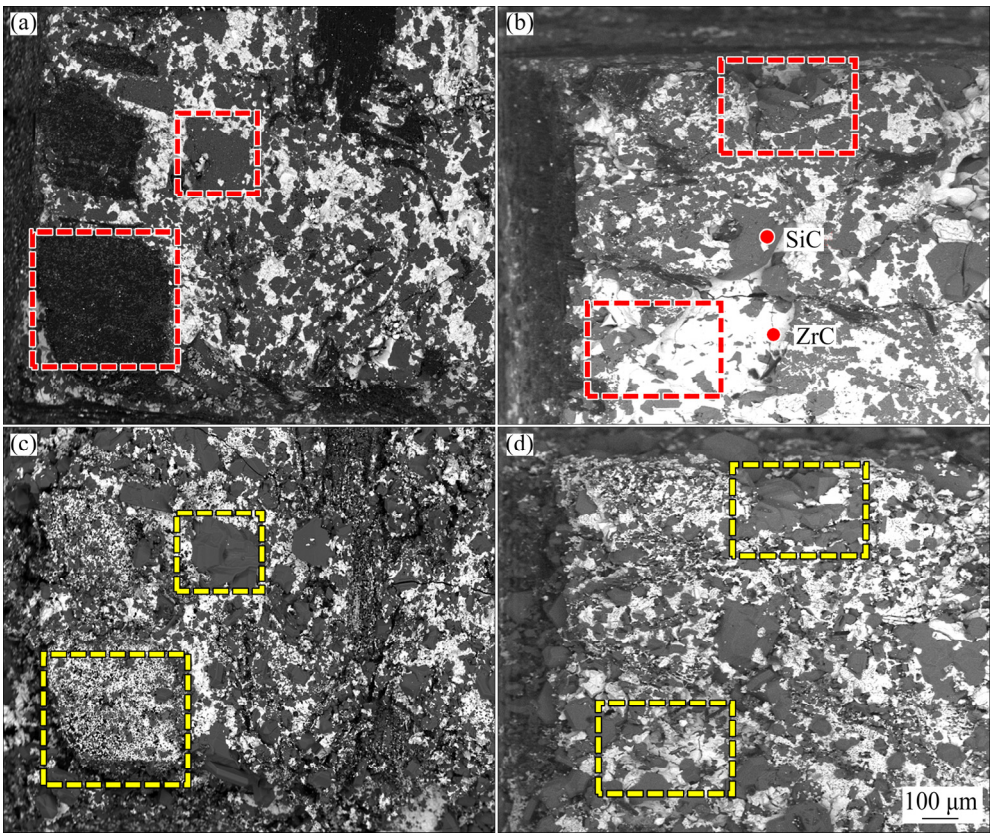

Fig. 9 SEM images of HSi21 and NaCl21 before and after high-temperature treatment: (a) HSi21 before thermal treatment; (b) NaCl21 before thermal treatment; (c) HSi21 after thermal treatment; (d) NaCl21 after thermal treatment

thermal treatment. From Figs. 9(a) and (c), it can be seen that after thermal treatment, the SiC phase in HSi21 sample experiences grain growth and crystal transformation, but the evolution degree is relatively low. Besides, unlike the exposed C fiber in the LSi21 (Figs. 4(a) and (c)), the surface of HSi21 is completely covered by a layer of ceramic phase. Especially, most of SiC grains in the calibrated area are fine, which is consistent with the large decrease of average grain size in HSi21. As the Zr−Si system modified C/C composites prepared by RMI inevitably contain Si residues, they would migrate from fiber bundle to surface through diffusion, then react with C to form fine-grained SiC, and finally affect the high-temperature thermal stability.

In the calibrated area of NaCl21 (Figs. 9(b) and (d)), only a small part of SiC grains show a growth trend and no α-SiC is observed, which is consistent with the XRD analysis.

Moreover, Table 2 shows the EPMA results of SiC phase in the calibrated areas of LSi21, HSi21,

and NaCl21 samples before and after thermal treatment. Before thermal treatment, the Si/C molar ratios of SiC in LSi21, HSi21 and NaCl21 are less than 1. This is because amorphous free C is dissolved in the SiC grains in the form of $Si_{1-x}C_{1+x}$ phase or distributed at the grain boundary, acting as diffusion barriers and having a positive effect on the stability of ceramic phase. After high-temperature treatment, the Si/C molar ratios of SiC in LSi21, HSi21, and NaCl21 all show upward trends. On the one hand, due to the decomposition of $Si_{1-x}C_{1+x}$ phase, the C atom diffuses out of crystal grain and thus decreases in the system [29]. On the other hand, because of the evaporation−condensation process, Si is concentrated on the surface of composites. In addition, with the Si content increasing in the infiltration masterbatch, the ascending range of Si/C molar ratio increases, which is the result of the more residual Si in the HSi21 composites. Furthermore, it is worth noting that after high-temperature treatment, the Si/C molar ratio of SiC in NaCl21 still remains less than 1 and the diffusion barrier effect of C does not disappear.

Table 3 shows the EPMA results of ZrC in the calibrated areas of LSi21, HSi21 and NaCl21 before and after thermal treatment. Before thermal treatment, the EPMA results reveal that the Zr/C molar ratios are less than 1 in the modified composites. According to the RMI mechanisms of C/C−ZrC−SiC composites, Si melts into the C/C pores and reacts with the pyrolytic C to form SiC, which prevents subsequent melt from directly contacting the pyrolytic C. Then, a large amount of free C diffuses into the melt and reacts with the low-melting Zr−Si alloy and forms ZrC and SiC. ZrC is a non-stoichiometric transition metal carbide whose chemical formula can be written as ZrC_x ($0.99>x>0.66$). Under normal conditions, it is in a "C-deficient" state with some C vacancies in its structure. Therefore, the free C is enriched in the ZrC grains or at the grain boundaries before high-temperature treatment. During high-temperature treatment, the Zr/C molar ratios of ZrC in the modified composites show an upward trend according to the EPMA results, approaching to 1. This result is ascribed to the outward diffusion of the free C which is dissolved in the ZrC grains or at the grain boundaries before treatment. In addition, as shown in Table 3, the change range of Si molar ratio in HSi21 is the largest, which further proves that as Si content in the infiltration masterbatch increases, the residual Si content in the modified composites increases. While, the change of Si in NaCl21 is small, which is attributed to the fact that NaCl can reduce the contents of residual Si and Zr−Si compounds in the modified composite during the RMI process [30].

3.3 High-temperature thermal stability mechanism

Figure 10 presents the thermal stability models for C/C−ZrC−SiC composites under different conditions. As shown in Fig. 10(a), the C/C−ZrC−SiC composites prepared by RMI method have complex structures and a rich variety of phases. To be specific, the phases contain SiC, ZrC, and some residual ZrSi, Si, C, etc.

Table 2 EPMA analysis results of SiC in LSi21, HSi21 and NaCl21

Sample	Content before treatment/at.%			Si/C molar ratio before treatment	Content after treatment/at.%			Si/C molar ratio after treatment
	Zr	C	Si		Zr	C	Si	
LSi21	0	52.91	47.09	0.89	0	48.10	51.90	1.08
HSi21	0	58.92	41.08	0.70	0	29.12	70.88	2.43
NaCl21	0	83.74	16.26	0.19	0	53.14	46.86	0.88

Table 3 EPMA analysis results of ZrC in LSi21, HSi21 and NaCl21

Sample	Content before treatment/at.%			Zr/C molar ratio before treatment	Content after treatment/at.%			Zr/C molar ratio after treatment
	Zr	C	Si		Zr	C	Si	
LSi21	29.27	70.0	0.73	0.42	34.76	63.34	1.91	0.55
HSi21	34.80	64.46	0.74	0.54	38.58	57.96	3.45	0.67
NaCl21	18.23	80.85	0.92	0.23	41.78	57.10	1.11	0.73

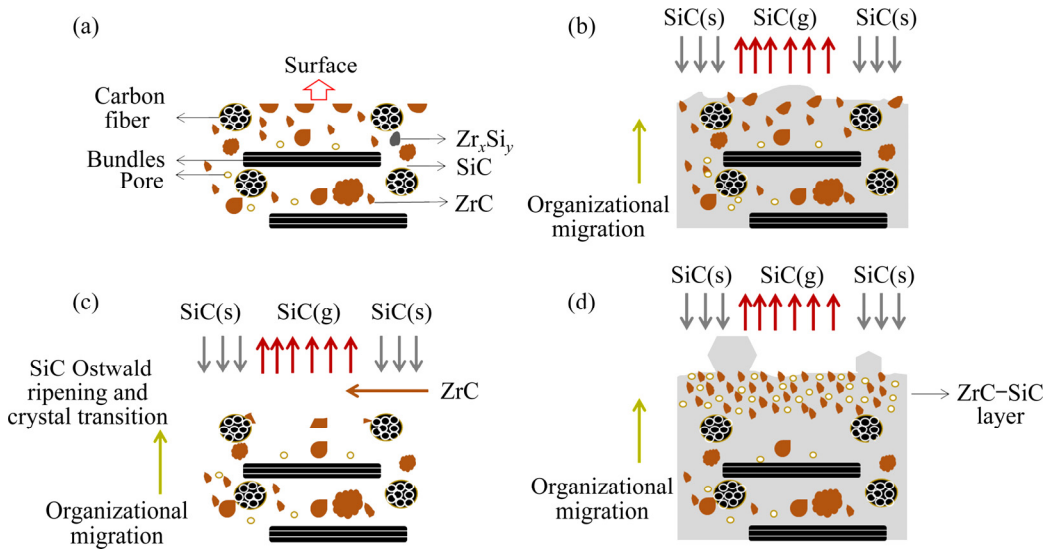

Fig. 10 Schematic diagrams of thermal stability models for C/C−ZrC−SiC composites: (a) Before thermal treatment; (b) After thermal treatment at 2000 °C for 3 h (LSi21); (c) After thermal treatment at 2300 °C for 3 h (LSi31); (d) After thermal treatment at 2000 °C for 24 h (LSi22)

When the thermal treatment temperature is above 2000 °C, the total surface energy of the composites increases owing to the difference of thermal expansion coefficients, and volume change factors such as the crystal transformation of SiC. At the same time, affected by high temperature, the surface of composite has high energies to adsorb large numbers of atoms and form the fine-grained SiC and ZrC, which will further increase the total surface energy. However, as we know, solids tend to minimize their surface energy. The mechanism for SiC to reduce the surface energy is Ostwald ripening. As evidenced in Fig. 4 and Fig. 7, both crystal transformation and Ostwald ripening of SiC are accompanied by volume changes and location migrations, which have great effects on the thermal stability of C/C−ZrC−SiC composites.

Figure 11 shows the schematic diagram of Ostwald ripening process [31]. As illustrated, there are three types of mechanisms: liquid-phase dissolution, evaporation–condensation, and solid-state diffusion. According to the Gibbs−Thompson formula (Eq. (7)), the relationship between the solubility and particle radius during Ostwald ripening process could be obtained as follows:

$$\ln\left(\frac{S_c}{S_\infty}\right)=\frac{\gamma\Omega}{kT}\left(\frac{1}{R_1}+\frac{1}{R_2}\right) \tag{7}$$

where S_c is the solubility of the curved solid surface, S_∞ is the solubility of the plane, γ is the surface energy, Ω is the atomic volume, k is the Boltzmann

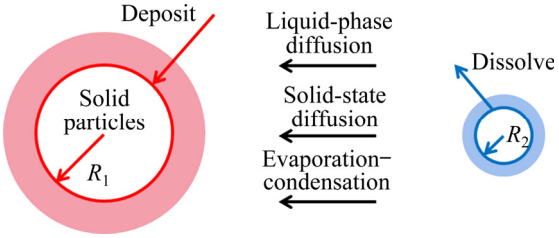

Fig. 11 Schematic diagram of Ostwald ripening process [31]

constant, and R_1 and R_2 are different atomic radii. Similarly, the relationship between the vapor pressure and atomic radius can be obtained according to the Kelvin equation (Eq. (8)):

$$\ln\left(\frac{P_c}{P_\infty}\right)=\frac{\gamma\Omega}{kT}\left(\frac{1}{R_1}+\frac{1}{R_2}\right) \tag{8}$$

where P_c is the vapor pressure of the curved solid surface, and P_∞ is the equilibrium vapor pressure of the plane.

The Ostwald ripening of SiC is related to its chemical potential. Because there are distinctions between size and volume for SiC grains in the composites prepared by RMI method, which leads to the differences in surface curvature and chemical potential for large and small particles. From Eqs. (7) and (8), it can be seen that the solubility or vapor pressure of small particles is greater than that of large particles [32]. Therefore, there is a net diffusion from small particles to large particles. In our system, large SiC particles absorb solute and

grow, while small particles continue to dissolve to compensate for the diffused solute. The final result is that large particles become larger, and small particles become smaller until they disappear, as shown in Fig. 10(b). In addition, because the melting point of each phase in the composites is relatively high and a sufficient melt environment is not formed at thermal treatment temperatures, the Ostwald ripening of SiC mainly depends on the solid-state diffusion and evaporation−condensation mechanisms.

For ZrC phase, it reduces the total surface energy by re-sintering behavior, which manifests that the single structure gradually merges to form a continuous and dense ceramic phase structure. The re-sintering of ZrC mainly depends on the surface diffusion, grain boundary diffusion, and bulk diffusion. These diffusions not only change the interplanar spacing of ZrC grains, but also change the morphology of the ceramic phase. To be specific, the surface diffusion results in the formation of typical layered accumulation structures on the surface of ZrC. Besides, grain boundary diffusion also plays a major role in the re-sintering behavior. When the grain boundary diffusion reaches the equilibrium between two adjacent ZrC grains, a hot-etched corner morphology will appear at the interface. What's more, bulk diffusion mainly relies on the C vacancies, which will lead to the grain migration. Meanwhile, the change of interplanar spacing is also affected by the residual internal stress. The high-temperature treatment weakens the interface bonding and reduces the residual internal stress in the composites.

In addition, increasing the thermal treatment temperature would increase the atom diffusion rate and the evaporation−condensation reaction rate. Therefore, compared with LSi21 at 2000 °C, the microstructure evolution and migration of SiC and ZrC in LSi31 at 2300 °C are more evident, as shown in Fig. 10(c). On the other hand, the extension of holding time will increase the degree of solid-state diffusion, so plenty of ceramic phases are enriched on the high-energy surface and a continuous ceramic layer is formed on the surface of LSi22 sample, as exhibited in Fig. 10(d). From the results of LSi31 and LSi22, it can be concluded that increasing temperature and extending holding time both affect the thermal stability of C/C−ZrC−SiC composites.

Furthermore, C/C−ZrC−SiC composites with high Si content have poorer thermal stability compared with low-Si systems, owing to the increased contents of SiC phase, low-melting Zr−Si alloy phase, and residual Si phase in the system. Besides, it is found that the addition of NaCl could form an ionic melt environment through the low-melting point molten salt, which promotes the formation of carbides, thereby eliminating the weak phases and having a positive effect on the thermal stability.

4 Conclusions

(1) The high-temperature thermal stability behavior of C/C−ZrC−SiC composites is characterized by macroscopic size and crystal structure, as well as microstructure evolution and location migration of ceramic phases.

(2) After thermal treatment in different conditions, the C/C−ZrC−SiC composites exhibit mass loss and thickness increase in varying degrees.

(3) The SiC phase has a great influence on the thermal stability of C/C−ZrC−SiC composites as it experiences Ostwald ripening and crystal transformation, accompanied by volume change and location migration. Meanwhile, the ZrC exhibits re-sintering behaviors with surface diffusion, grain boundary diffusion, and bulk diffusion during thermal treatment.

(4) The effect of increasing temperature is more remarkable on the thermal stability of C/C−ZrC−SiC composites than that of extending holding time.

Acknowledgments

This work was supported by the National Natural Science Foundation of China (No. U19A2099), the CAS Key Laboratory of Carbon Materials, China (No. KLCMKFJJ2005), and the Fund of Aerospace Research Institute of Material and Processing Technology, China (No. 6142906200108).

References

[1] FU Yan-qin, ZHANG Yu-lei, ZHANG Jian, LI Tao, CHEN Guo-hui. Mechanical properties and ablation resistance of HfC nanowire modified carbon/carbon composites [J]. Ceramics International, 2020, 46: 16142−16150.

[2] SQUIRE T H, MARSCHALL J. Material property

requirements for analysis and design of UHTC components in hypersonic applications [J]. Journal of the European Ceramic Society, 2010, 30: 2239−2251.

[3] LI Qing-gang, DONG Shao-ming, WANG Zhi, SHI Guo-pu. Fabrication and properties of 3-D Cf/ZrB_2−ZrC−SiC composites via polymer infiltration and pyrolysis [J]. Ceramics International, 2013, 39: 5937−5941.

[4] WANG Dong, WANG Yu-jin, RAO Jian-cun, OUYANG Jia-hu, ZHOU Yu, SONG Gui-ming. Influence of reactive melt infiltration parameters on microstructure and properties of low temperature derived C_f/ZrC composites [J]. Materials Science and Engineering A, 2013, 568: 25−32.

[5] ZOU L H, WALI N, YANG J, P BANSAL N. Microstructural development of a C_f/ZrC composite manufactured by reactive melt infiltration [J]. Journal of the European Ceramic Society, 2010, 30: 1527−1535.

[6] CHANG Ya-bin, SUN Wei, XIONG Xiang, CHEN Zhao-ke, WANG Ya-lei, HAO Zhen-hua, XU Yong-long. Microstructure and ablation behaviors of a novel gradient C/C−ZrC−SiC composite fabricated by an improved reactive melt infiltration [J]. Ceramics International, 2016, 42: 16906−16915.

[7] LI Zhao-qian, LI He-jun, ZHANG Shou-yang, WANG Jie, LI Wei, SUN Feng-jiao. Effect of reaction melt infiltration temperature on the ablation properties of 2D C/C−SiC−ZrC composites [J]. Corrosion Science, 2012, 58: 12−19.

[8] XU Yong-long, SUN Wei, XIONG Xiang, PENG Zheng, CHEN Yun-tian, HAO Zhen-hua. Microstructure and properties of ZrC−SiC multi-phase coatings prepared by thermal evaporation deposition and an in-situ reaction method [J]. Surface and Coatings Technology, 2018, 349: 797−806.

[9] LIU Chun-xuan, SU Zhe-an, HUANG Qi-zhong, CHEN Jian-xun, YANG Xin, CAO Liu-xu, YIN Teng, ZHONG Ping. Ablation behavior of ZrC−SiC coated C/C−ZrC−SiC composites prepared by precursor infiltration pyrolysis combined with reactive melt infiltration [J]. Journal of Alloys and Compounds, 2014, 597: 236−242.

[10] YANG Xin, SU Zhe-an, HUANG Qi-zhong, FANG Xiao, CHAI Li-yuan. Microstructure and mechanical properties of C/C−ZrC−SiC composites fabricated by reactive melt infiltration with Zr, Si mixed powders [J]. Journal of Materials Science & Technology, 2013, 29: 702−710.

[11] CHEN Bo-wen, NI De-wei, WANG Jing-xiao, JIANG You-lin, DING Qi, GAO Le, ZHANG Xiang-yu, DING Yu-sheng, DONG Shao-ming. Ablation behavior of C_f/ZrC−SiC-based composites fabricated by an improved reactive melt infiltration [J]. Journal of the European Ceramic Society, 2019, 39: 4617−4624.

[12] CHEN Si-an, HU Hai-feng, ZHANG Yu-di, ZHANG Chang-rui, WANG Qi-kun. Effects of high-temperature annealing on the microstructure and properties of C/SiC−ZrB_2 composites [J]. Materials & Design, 2014, 53: 791−796.

[13] MEI Hui, ZHANG Hui, HUANG Wei-zhao, HAN Ming, XU Ya-wei, CHENG Lai-fei. Effects of heat treatment temperatures on microstructures and mechanical properties of the chopped carbon fibres SiC composites [J]. Advances in Applied Ceramics, 2018, 117: 389−394.

[14] QIN Yan-fang, ZHAO Hong-jian, LI Chao, LU Jin-bin, HE Ji-ning. Effect of heat treatment on the microstructure and corrosion behaviors of reactive plasma sprayed TiCN coatings [J]. Surface and Coatings Technology, 2020, 398: 126086.

[15] ZHANG Tai-quan, WANG Yu-jin, ZHOU Yu, SONG Gui-ming. Effect of heat treatment on microstructure and mechanical properties of ZrC particles reinforced tungsten-matrix composites [J]. Materials Science and Engineering A, 2009, 512: 19−25.

[16] WEI Bo-xin, WANG Dong, WANG Yu-jin, ZHANG Hai-bin, PENG Shu-ming, XU Can-hui, SONG Gu-ming, ZHOU Yu. Corrosion kinetics and mechanisms of ZrC_{1-x} ceramics in high temperature water vapor [J]. RSC Advances, 2018, 8: 18163−18174.

[17] LI Y, KATSUI H, GOTO T. Effect of heat treatment on the decomposition of TiC−ZrC solid solutions by spark plasma sintering [J]. Journal of the European Ceramic Society, 2016, 36: 3795−3800.

[18] CHEN Si-an, JI Hong-liang, LI Yong, LI Guang-de, MEI Min, HU Hai-feng. Effects of high-temperature annealing on the microstructure and properties of C/ZrC composites prepared by reactive melt infiltration [J]. Materials Science and Engineering A, 2017, 686: 41−45.

[19] ZHOU Xin-gui, ZHOU Chang-cheng, ZHANG Chang-rui, CAO Ying-bin, ZOU Shi-qin. Effect of heat treatment on the microstructure and mechanical properties of C_f/SiC composites [J]. Key Engineering Materials, 2007, 336: 1291−1293.

[20] YU Yi-ping, WANG Song, LI Wei, JIANG Jin-ming. Effect of ultra-high temperature heat treatment on microstructures of W/ZrC cermets fabricated by different routes [J]. Rare Metal Materials and Engineering, 2017, 46: 63−67.

[21] JIA Peng. Solution and ageing behavior of W−30ZrC composites [D]. Harbin: Harbin Institute of Technology, 2011. (in Chinese)

[22] XIE R J, MITOMO M, KIM W, KIM Y W, ZHAN G D, AKIMUNE Y. Phase transformation and texture in hot-forged or annealed liquid-phase-sintered silicon carbide ceramics [J]. Journal of the American Ceramic Society, 2004, 85: 459−465.

[23] QIU Hai-peng, HAN Li-jun, LIU Lang. Properties and microstructure of graphitised ZrC/C or SiC/C composites [J]. Carbon, 2005, 43: 1021−1025.

[24] ZHAN G D, XIE R J, MITOMO M, KIM Y W. Effect of β-to-α phase transformation on the microstructural development and mechanical properties of fine-grained silicon carbide ceramics [J]. Journal of the American Ceramic Society, 2001, 84: 945−950.

[25] BOOTSMA G A, KNIPPENBERG W F, VERSPUI G. Phase transformations, habit changes and crystal growth in SiC [J]. Journal of Crystal Growth, 1971, 8: 341−353.

[26] VOORHEES P W. The theory of Ostwald ripening [J]. Journal of Statistical Physics, 1985, 38: 231−252.

[27] LLER R K. The chemistry of silica [M]. New York: John Wiley and Sons, 1979.

[28] XU Yong-long, SUN Wei, XIONG Xiang, LIU Fu-qun, LUAN Xin-gang. Ablation characteristics of mosaic structure ZrC−SiC coatings on low-density, porous C/C

composites [J]. Journal of Materials Science & Technology, 2019, 35: 2785−2798.
[29] MA Yan, WANG Song, CHEN Zhao-hui. Raman spectroscopy studies of the high-temperature evolution of the free carbon phase in polycarbosilane derived SiC ceramics [J]. Ceramics International, 2010, 36: 2455−2459.
[30] XU Yong-long, SUN Wei, XIONG Xiang, LIU Fu-qun, MIAO Chun-mao. Chloride salt assisted reactive molten infiltration method for C_f−UHTCs and their unique microstructure [J]. Ceramics International, 2020, 46: 6424−6435.
[31] BROCK S L. Nanostructures and nanomaterials: Synthesis, properties and applications [J]. Journal of the American Ceramic Society, 2004, 126: 549−549.
[32] VOOK R W. Structure and growth of thin films [J]. International Metals Reviews, 1982, 27: 209−245.

基于区域标记法的 C/C−ZrC−SiC 复合材料的高温热稳定性能

彭 峥[1]，苗春茂[1]，孙 威[1]，徐永龙[1]，陈海坤[2]，刘宇峰[2]，张红波[1]，熊 翔[1]

1. 中南大学 粉末冶金国家重点实验室，长沙 410083；
2. 航天材料与工艺研究所 先进功能复合材料技术重点实验室，北京 100089

摘 要：为研究陶瓷基复合材料的热稳定性，采用反应熔渗法制备 3 种不同 Zr/Si 摩尔比的 C/C−ZrC−SiC 复合材料，并结合区域标记法系统研究复合材料在不同热处理温度和保温时间下的热稳定性。结果显示，低硅复合材料的质量损失率随温度升高呈递增趋势，并且复合材料中 β-SiC 相转变为 α-SiC 相。在标记区域中 SiC 相发生 Ostwald 熟化，其微观结构的体积和位置均发生改变，而 ZrC 相经历再烧结过程。此外，升高温度比延长保温时间对复合材料的热稳定性具有更加显著的影响，主要是因为温度升高使原子具有更快的扩散速率。

关键词：热稳定性；陶瓷基复合材料；反应熔渗法；高温热处理；区域标记法

(Edited by Wei-ping CHEN)